

# A Test of Thick-Target Nonuniform Ionization as an Explanation for Breaks in Solar Flare Hard X-ray Spectra

Yang Su<sup>1,2,3</sup>

yangsu@helio.gsfc.nasa.gov

Gordon D. Holman<sup>1</sup>

Brian R. Dennis<sup>1</sup>

Anne K. Tolbert<sup>1,4</sup>

and

Richard A. Schwartz<sup>1,2</sup>

Received \_\_\_\_\_; accepted \_\_\_\_\_

---

<sup>1</sup>NASA Goddard Space Flight Center, Solar Physics Laboratory, Code 671, Greenbelt, MD 20771

<sup>2</sup>Department of Physics, The Catholic University of America, Washington, DC 20064

<sup>3</sup>Purple Mountain Observatory, Nanjing, China 210008

<sup>4</sup>Wyle IS, McLean, VA 22102

## ABSTRACT

Solar nonthermal hard X-ray (HXR) flare spectra often cannot be fitted by a single power law, but rather require a downward break in the photon spectrum. A possible explanation for this spectral break is nonuniform ionization in the emission region. We have developed a computer code to calculate the photon spectrum from electrons with a power-law distribution injected into a thick-target in which the ionization decreases linearly from 100% to zero. We use the bremsstrahlung cross-section from Haug (1997), which closely approximates the full relativistic Bethe-Heitler cross-section, and compare photon spectra computed from this model with those obtained by Kontar, Brown and McArthur (2002), who used a step-function ionization model and the Kramers approximation to the cross-section. We find that for HXR spectra from a target with nonuniform ionization, the difference ( $\Delta\gamma$ ) between the power-law indexes above and below the break has an upper limit between  $\sim 0.2$  and  $0.7$  that depends on the power-law index  $\delta$  of the injected electron distribution. A broken power-law spectrum with a higher value of  $\Delta\gamma$  cannot result from nonuniform ionization alone. The model is applied to spectra obtained around the peak times of 20 flares observed by the Ramaty High Energy Solar Spectroscopic Imager (*RHESSI*) from 2002 to 2004 to determine whether thick-target nonuniform ionization can explain the measured spectral breaks. A Monte Carlo method is used to determine the uncertainties of the best-fit parameters, especially on  $\Delta\gamma$ . We find that 15 of the 20 flare spectra require a downward spectral break and that at least 6 of these could not be explained by nonuniform ionization alone because they had values of  $\Delta\gamma$  with less than a 2.5% probability of being consistent with the computed upper limits from the model. The remaining 9 flare spectra, based on this criterion, are consistent with the nonuniform ionization model.

*Subject headings:* Sun: flares — Sun: X-rays, gamma rays — Sun: chromosphere

## 1. Introduction

Knowledge of the energy distribution of energetic electrons in solar flares is important for establishing the total energy deposited in accelerated electrons, constraining possible acceleration mechanisms, understanding electron propagation and energy losses, and establishing the relationships between flare X-ray and  $\gamma$ -ray sources, radio sources, and solar energetic particle (SEP) events. It is widely accepted that electrons are accelerated in the corona, propagate along the legs of magnetic loops to the lower atmosphere, where they interact to produce thick-target bremsstrahlung emission (Brown 1971). In the simplest case, the photon spectrum has an approximately single power-law form if the electrons have a single power-law energy distribution. However, hard X-ray observations often show broken power-law features in the spectra (e.g., Dulk et al. 1992; Lin & Schwartz 1987). During the rising phase of a flare, the X-ray spectra may evolve from a single power-law to a broken power-law with a break energy that is typically between  $\sim 50$  and 150 keV (Dulk et al. 1992).

Various processes can produce such breaks in the X-ray spectrum. Processes that affect the count rate or photon spectra directly include the following:

- (a) Instrumental effects, such as pulse pile-up (Smith et al. 2002) and non-solar background counts in the detectors.
- (b) Additional components, such as albedo, X-ray photons reflected at the solar photosphere (Kontar et al. 2006; Kontar & Brown 2006; Zhang & Huang 2004), and emission from thermal plasma.

Processes that affect the photon spectra indirectly through changes in the distribution of the accelerated electrons include the following:

- (a) A non-power-law electron distribution from the acceleration process, e.g., a double power-law electron distribution, a low-energy cutoff (Gan et al. 2002; Sui et al. 2007), or a high-energy cutoff (Holman 2003).
- (b) An anisotropic electron pitch-angle distribution (Petrosian 1973; Massone et al. 2004).
- (c) Beam-plasma instabilities that can flatten or, more generally, introduce breaks into the electron energy distribution (e.g. Holman et al. 1982; Melrose 1990).
- (d) Return current energy losses (Knight & Sturrock 1977; Zharkova & Gordovskyy 2006).
- (e) Nonuniform target ionization (Brown 1973; Brown et al. 1998; Kontar et al. 2002).

In this paper, we focus only on nonuniform ionization in the thick-target region. The long-range collisional energy losses of energetic electrons are lower (by a factor of up to 2.8, see Brown (1973)) in un-ionized or partially ionized plasma than in fully ionized plasma. The electron-proton bremsstrahlung cross-section, on the other hand, is unaffected by the state of ionization. Thus, the hard X-ray bremsstrahlung emission is relatively enhanced at energies above that at which the emitting electrons penetrate to a depth in the chromosphere where the plasma is no longer fully ionized. The photon spectrum from the whole target is then no longer a single power-law for an input of electrons with a single power-law distribution.

Kontar et al. (2002) used a simple step-function model to describe the ionization distribution of the solar atmosphere in which the plasma is fully ionized above a certain altitude and un-ionized below. The fit functions (*f\_ion.pro* and *ion\_fit.pro*) contained in the Solar SoftWare (SSW) package are easy and convenient to use in OSPEX, the spectral analysis component of the *RHESSI* software package. However, the Kramers cross-section used by this fitting function to obtain the photon spectrum  $I_{Kr}(\varepsilon)$  is only an approximation to the bremsstrahlung cross-section (Brown et al. 2008). In our new program, we use the

more accurate approximation given by Haug (1997) to the relativistic Bethe-Heitler cross-section to obtain  $I_H(\varepsilon)$ . This is already incorporated in the thick-target function in OSPEX (see also “Thick-Target Bremsstrahlung Code Documentation” by G. D. Holman and Y. Su, located at [http://hesperia.gsfc.nasa.gov/ssw/packages/xray/doc/brm\\_thick\\_doc.pdf](http://hesperia.gsfc.nasa.gov/ssw/packages/xray/doc/brm_thick_doc.pdf)). Furthermore, our program includes the possibility of a linear decrease in the ionization distribution from 100% to 0% ionization (Section 2).

In Section 3, we analyze the spectral break resulting from this nonuniform ionization model. We show that the energy dependence of the spectral index  $\gamma$  of the photon spectrum computed from the model has a valley centered near the energy  $E_*$  at which the electrons stop at the column depth where the ionization changes. The difference between the maximum and the minimum value of  $\gamma$  determined in this way can be used as an upper limit on  $\Delta\gamma_{data}$ , defined as the difference of the two indexes  $\gamma_1$  and  $\gamma_2$  in a broken power-law fit to the spectrum. This gives us a way to rule out nonuniform ionization being the sole cause of the measured spectral breaks.

We study a sample of flares observed by the Ramaty High Energy Solar Spectroscopic Imager (*RHESSI*) to assess the ability of the nonuniform ionization model to explain measured spectral breaks. With *RHESSI*’s high X-ray spectral resolution (Lin et al. 2002), and the large database of flares recorded since 2002, we can determine the number of flares in the sample that have broken power-law spectra and the number of those with  $\Delta\gamma$  greater than the upper limit and hence cannot be explained by nonuniform target ionization alone. The flare sample is described in Section 4 and the results of the study are given in Section 5. A Monte Carlo method used to determine the uncertainties on the fit parameters and  $\Delta\gamma_{data}$  is also described in Section 5. Our conclusions are given in Section 6.

## 2. Nonuniform Ionization Models

The step-function ionization profile used by Kontar et al. (2002) assumes that the plasma (pure hydrogen) is fully ionized above a given altitude and fully un-ionized below. Our linear-function includes a region in which the fractional ionization decreases linearly from 1 to 0 with increasing column density  $N$  (in units of  $\text{cm}^{-2}$ ) for electrons traveling down from the corona into the chromosphere. We define  $N_1$  as the column density at which the ionization level begins to decrease and  $N_0$  that at which it reaches zero. Thus, the atmospheric fractional ionization  $x(N)$  is given by the expression:

$$x(N) = \begin{cases} 1, & N < N_1 \\ \frac{N_0 - N}{N_0 - N_1}, & N_1 \leq N \leq N_0 \\ 0, & N > N_0. \end{cases} \quad (1)$$

When  $N_0 = N_1 \equiv N_*$ , this reduces to the step-function ionization distribution.

Following Brown et al. (1996), an effective column density  $M$  can be defined such that

$$E_e^2 - E^2 = 2K'M = 2K' \int_0^N (\lambda + x(N')) dN', \quad (2)$$

where,  $K' = 2\pi e^4 \Lambda$ ,  $\Lambda = \Lambda_{ee} - \Lambda_{eH} \simeq 17$ ,  $\lambda = \Lambda_{eH}/\Lambda \simeq 0.55$  (Brown 1973), and  $E_e$  is the initial energy of the electron.  $\Lambda$  and  $\lambda$  are set to these values for all the models in this paper.

From Equation (2), we derive the energies  $E_1$  and  $E_0$ , the initial energies of electrons that lose all of their energy at column depths  $N_1$  ( $M_1$ ) and  $N_0$  ( $M_0$ ), respectively, and obtain the relation between  $N$  in the range from  $N_1$  to  $N_0$  and  $E$  (energy of electron at  $N$ )

for an electron with initial energy  $E_e$ :

$$\begin{aligned}
 E_1^2 &= 2K'(\lambda + 1)N_1 \\
 E_0^2 &= K'(2\lambda + 1)N_0 + K'N_1 \\
 N(E_e, E) &= (N_0 - N_1)\lambda + N_0 \\
 &\quad - \left[ [(N_0 - N_1)\lambda + N_0]^2 - N_1^2 - \frac{(E_e^2 - E^2)(N_0 - N_1)}{K'} \right]^{\frac{1}{2}}.
 \end{aligned} \tag{3}$$

These expressions are used below to compute the thick-target bremsstrahlung spectrum. Notice that an electron of energy  $E$  greater than  $E_1$  stops at the same effective column density  $M$  but different column densities  $N$  in the step-function and linear-function models.

The bremsstrahlung cross-section for a hydrogen atmosphere can be written as  $Q(\varepsilon, E) = \frac{Q_0}{\varepsilon E} q(\varepsilon, E)$ , where  $Q_0$  is a constant and  $\varepsilon$  is the photon energy. For the Kramers approximation  $q(\varepsilon, E) = 1$ . For our study, we used the Haug (1997) cross-section, which closely approximates the full relativistic cross-section of Bethe and Heitler (equation 3BN of Koch & Motz 1959).

Based on equations (1) and (3), the thick-target photon flux at the Earth for the linear ionization function in units of photons  $\text{s}^{-1} \text{ cm}^{-2} \text{ keV}^{-1}$  is

$$\begin{aligned}
 I_{linear}(\varepsilon) &= \frac{Q_0}{4\pi(AU)^2 K' \varepsilon} \int_{\varepsilon}^{\infty} q(\varepsilon, E) \left[ \int_E^{(E^2 + E_1^2)^{1/2}} \frac{\mathcal{F}_e(E_e)}{\lambda + 1} dE_e \right. \\
 &\quad + \int_{(E^2 + E_1^2)^{1/2}}^{(E^2 + E_0^2)^{1/2}} \frac{\mathcal{F}_e(E_e)}{\lambda + \frac{N_0 - N(E_e, E)}{N_0 - N_1}} dE_e \\
 &\quad \left. + \int_{(E^2 + E_0^2)^{1/2}}^{\infty} \frac{\mathcal{F}_e(E_e)}{\lambda} dE_e \right] dE,
 \end{aligned} \tag{4}$$

where AU is the distance from the Sun to the Earth (in cm) and  $\mathcal{F}_e(E_e)$  is the injected electron flux distribution function (electrons  $\text{s}^{-1} \text{ keV}^{-1}$ ). The center term of the part of the equation in square brackets describes the region in which the ionization changes linearly. When  $E_1 = E_0 \equiv E_*$ , this term is zero and Equation (4) becomes the step function result in Equation (4) of Kontar et al. (2002).



For a single-power-law electron flux distribution with a low-energy cutoff at  $E_c$ ,

$$\mathcal{F}_e(E_e) = (\delta - 1) \frac{\mathcal{F}_c}{E_c} \left[ \frac{E_e}{E_c} \right]^{-\delta}. \quad (5)$$

$\mathcal{F}_c$  is the integrated electron flux above  $E_c$  ( $10^{35}$  electrons  $\text{s}^{-1}$  in this study) and  $\delta$  the power-law index of the electron distribution. In this paper, the low-energy cutoff  $E_c$  is set to 1 keV and, therefore, does not affect the shape of the spectra. A high-energy cutoff is set to 10 MeV in our calculations, a value high enough so that it has no significant impact on the spectra in the energy range of interest below 200 keV.

The top and middle panels of Figure 1 show a comparison of the computed photon spectra derived from this single-power-law electron distribution with  $\delta = 4$  for five models, three with nonuniform ionization and two with uniform ionization. The three models with nonuniform ionization are (1) the linear-ionization function with the full cross-section for  $E_1=30$  keV and  $E_0=60$  keV (thick line), (2) step-function ionization with the full cross-section and  $E_*=30$  keV (dashed line), and (3) step-function ionization with the Kramers cross-section and  $E_*=30$  keV (dotted line). The column densities for these values of  $E_1$ ,  $E_0$ , and  $E_*$ , obtained from Equation (3) are  $N_* = N_1 = 1.3 \times 10^{20} \text{ cm}^{-2}$  and  $N_0 = 7.1 \times 10^{20} \text{ cm}^{-2}$ . These are compared with the identically shaped curves (the solid line) for (4) a fully ionized plasma (thin solid line) and (5) an un-ionized plasma (long dashed line). For these two curves the values of  $\gamma$  are identical at each energy but the flux from nonthermal electrons in the ionized plasma is a factor of  $(\lambda + 1)/\lambda = 2.8$  smaller (Brown 1973), as shown in Equation 4 and Figures 1 and 2. For the nonuniform ionization models, the emission at energies  $\gtrsim 10$  keV becomes significantly greater than that for the fully ionized thick-target model and gets closer to the un-ionized thick-target model. The linear-ionization model (1) lies between the step-function model (2) and the fully ionized model (4). The bottom panel gives the percentage difference between the step-function results with the two cross-sections ( $I_H$  and  $I_{Kr}$ ) as a function of photon energy  $\varepsilon$ . The

difference reaches 36% at 3 keV, falls to 18% at 50 keV and changes sign at 190 keV.

Figure 2 shows the spectral index  $\gamma$  of photon spectra as a function of  $\varepsilon$  for the five models in Figure 1. Note that in Figures 1 and 2 the indexes for the fully ionized model (4) and un-ionized model (5) with full cross-section (thin solid lines) are not the constant value of  $\gamma = \delta - 1 = 3$ , obtained from computations with the Kramers or non-relativistic Bethe-Heitler cross-section (Brown 1971). Instead  $\gamma$  changes slowly with photon energy from a value of 3.07 at 6 keV to a maximum value of 3.14 at 82 keV and decreasing to a value of 2.95 at 500 keV. This is consistent with the results obtained by Holman (2003) and is caused by the use of the full, relativistic cross-section (also see Brown et al. 2008). The middle panel shows the derivative of  $\gamma(\log_{10}\varepsilon)$ ,  $\gamma'(\log_{10}\varepsilon) = d\gamma(\log_{10}\varepsilon)/d(\log_{10}\varepsilon)$ , for the step-function model with full cross-section. The energy of the upward knee in the spectrum, defined by  $\gamma'_{min} = -0.6$ , is at 6 keV and the downward knee ( $\gamma'_{max}=0.8$ ) is at 38 keV. The bottom panel of Figure 2 gives the percentage difference in  $\gamma$  as a function of photon energy obtained with the step-function ionization models with the two different cross-sections. The maximum difference of  $\sim 6.8\%$  occurs at 33 keV.

The photon spectra from the linear-ionization model with  $E_1 = 30$  keV and three different  $E_0$  values (40, 50, and 60 keV) are shown in Figure 3. They are compared with the step-function model for  $E_* = 30$  keV (thin line). As  $E_0$  increases, the photon flux at a given energy  $\varepsilon$  decreases because the average ionization level as seen by the electrons with energies above  $E_1$  increases.

### 3. Maximum Spectral Break

We have shown that the index  $\gamma$  of the X-ray photon spectrum derived from nonuniform ionization models changes significantly with photon energy. The spectra show the expected

upward knee at energies below the minimum of the spectral index and the downward knee above this minimum (see the top panel of Figure 2). As pointed out by Brown (1973) and Kontar et al. (2002), the upward knee (at  $\sim 6$  keV in Figure 2) is likely to be masked by thermal emission, but the downward knee can be observed in flare spectra. We consider the changes of index at different photon energies and compare that with the observations.

The question is to what degree will the photon spectrum be flattened due to nonuniform ionization. If we use a simple broken power-law function to fit the spectrum, the two indexes,  $\gamma_1$  below and  $\gamma_2$  above the break energy, are estimates of the average values of  $\gamma(\varepsilon)$  over the two energy ranges separated by the break energy. On the other hand,  $\gamma(\varepsilon)$  shows the change of index with photon energy. The difference between the maximum and minimum values of  $\gamma$  for energy range 3 to 200 keV from the model gives an upper limit on  $\Delta\gamma_{data} = \gamma_2 - \gamma_1$ . Therefore, comparing  $\Delta\gamma_{data}$  with the maximum change of  $\gamma$ ,  $\Delta\gamma_{model} (= \gamma_{max} - \gamma_{min})$ , predicted by the model provides us with a simple way of testing the validity of the model. However, an  $E_*$  that is below the thermal energy or above the observed photon energy, or a limited photon energy range will not show the entire change of  $\gamma$  above the thermal energy, resulting in a smaller value of  $\Delta\gamma_{data}$ . Thus, the  $\Delta\gamma_{model}$  we used here is the true upper limit from the model. Any spectrum with  $\Delta\gamma_{data}$  larger than  $\Delta\gamma_{model}$  is not consistent with the model.

The solid curve in Figure 4 shows the maximum change of  $\gamma$ , i.e.,  $\Delta\gamma_{model}$ , caused by the step-function nonuniform ionization model with the full cross-section  $I_H$ , as a function of  $\delta$ . It indicates that  $\Delta\gamma_{model}$  becomes larger for a steeper electron distribution. It does not change with  $E_*$ .

These results show that the spectral break caused by nonuniform ionization in the thick-target has an upper limit on  $\Delta\gamma_{data}$ . For example, electrons with a single power-law distribution index  $\delta$  of 4 cannot generate a photon spectrum with a  $\Delta\gamma_{data} > 0.44$ . A photon

spectrum with a  $\Delta\gamma_{data}$  that is larger than this limit cannot be explained by nonuniform ionization alone.

The linear ionization model gives a smaller value of  $\Delta\gamma_{model}$  than the step-function model (see Figures 1 and 2). This is expected since the step-function ionization model is the limiting case of the more gradual linear model. Therefore, we only use the step-function model in the following analysis of flare spectra.

#### 4. RHESSI Flare Sample

We selected a sample of flares from the RHESSI database to test the hypothesis that the spectral break in the nonthermal part of the flare X-ray spectra can be explained by nonuniform ionization in the thick-target region. The following selection criteria were used:

- 1) Flares were selected in the period between the start of the *RHESSI* observations on 2002 February 12 and 2004 December 31. The end date was chosen to provide a manageable sample size and to avoid including flares observed with somewhat degraded spectral resolution resulting from radiation damage to the germanium detectors. Non-solar and particle events were excluded to give a total of 7815 events.
- 2) Only flares with a 12-25 keV count rate greater than 300 counts s<sup>-1</sup> detector<sup>-1</sup> were included. We also required the 50-100 keV count rate to be at least  $3\sigma$  above the background count rate. These criteria ensure adequate count rates to obtain useful spectral fits. The number of events decreased to 83.
- 3) Only flares located at a radial distance of at least 927'' from disk center (corresponding to 75 degrees longitude at the solar equator) were selected. This minimizes the impact of albedo on the X-ray spectrum (Kontar et al. 2006). Even so, we always corrected

the spectra for albedo from isotropically emitted photons. This reduced the number of events to 22.

- 4) The corrected livetime counter was required to be greater than 90% during the HXR peak of the flare. This minimizes the impact of pulse pile-up (Smith et al. 2002; Kašparová et al. 2007). This gave a final sample of 20 flares.

## 5. Spectral Analysis

We used 1/3 keV energy bins from 3 to 15 keV, 1 keV bins between 15 keV and 50 keV, 5 keV bins between 50 to 100 keV and 10 keV bins above 100 keV (i.e. binning code 22 in OSPEX). This ensures each energy bin in our fit range has more than 10 counts. The accumulation time for the spectra was taken to be one spin period ( $\sim 4$  s) at the HXR (25-50 keV) peak time. We used data from the front segments of all *RHESSI* detectors, excluding 2 and 7 for their relatively poor energy resolution (and 5 for the flare that occurred on 30 Nov 2003 due to its unusually low livetime, and 8 for some of the flares due to interference from *RHESSI*'s communication antenna). The full *RHESSI* response matrix was used for the spectral fits. Following Sui et al. (2007), we set the instrumental systematic uncertainty to zero for obtaining spectral fits. Pixon images were made at 40-60 keV for the same time intervals to show the HXR source structure.

Estimating the non-flare background spectrum is important for *RHESSI* spectral fitting, especially at high energies where the flare and background count rates can be comparable. We used time intervals before and after the flaring time if the background appeared constant. If the attenuator state changed during a flare, we used data from the proceeding and/or following orbital night for background. If the flare occurred on the tail of another flare or had some other background complication, then a higher order background

fit was derived from the light curve before and after the flaring time, or a combination of night-time data at low energies and background information at high energies was used.

To get the best-fit spectral parameters, we used a sum of spectral models that included an isothermal model (CHIANTI version 5.2) for the continuum thermal emission, three gaussians for the thermal and instrumental line complexes, and one of three different functions for the nonthermal part. The measured count-rate spectra were fitted above 6 keV (above 15 keV if the attenuator state was A3), up to an energy that is determined for each flare by the photon energy at which the background emission becomes significant, with a minimum upper limit of 70 keV and a maximum upper limit of 200 keV. Three spectral lines were used when needed: the iron line complex at  $\sim 6.7$  keV, the iron/nickel line complex at  $\sim 8$  keV (Phillips 2004) combined with an instrumental line at  $\sim 8.5$  keV, and an instrumental line at  $\sim 10.5$  keV. The three functions used for the nonthermal emission were a double power-law photon spectrum and two thick-target step-function ionization models,  $I_{Kr}$  and  $I_H$ . Table 1 shows the fit results for these flares. The reduced  $\chi^2$  for each fit is given in the table.

To determine the uncertainty on each parameter of our fit functions, especially on  $\Delta\gamma_{data}$ , we used a Monte Carlo method. First, we obtained best-fit parameters by fitting the measured count rate spectra in OSPEX. Then we added background to the expected count flux (model flux) and used the Monte Carlo method to randomly vary the total counts in each energy bin following a Poisson distribution. Then the new count-rate spectrum was fitted again to get new best-fit parameters. By repeating these steps 2000 times, we obtained a probability distribution for each parameter. The uncertainty on each parameter was then determined from the 95% confidence interval (about  $2\sigma$ ) of the distribution. We found that the probability distribution is usually not symmetrical, so we determined the 95% confidence interval by calculating where 2.5% of the distribution is in each tail. One

example for the distribution of  $\Delta\gamma_{data}$  is shown in Figure 5. The two dashed lines give the 95% confidence interval and the dotted line gives the upper limit  $\Delta\gamma_{model}$  (from Figure 4) for this flare (No.5 in Table 1).

The background subtraction also introduces some uncertainty in the derived spectral indexes. The uncertainty is primarily in  $\gamma_2$ , since the high-energy part of the spectrum becomes comparable to the background level. We used different but reasonable background models for each flare to check the influence of the background on the fit results and found that 14 of the 15 flares (see Table 1) requiring a double-power-law fit do not have significant changes in  $\gamma_2$  (the changes are all smaller than 0.02). Only flare No. 14 has an increase of about 0.06, which gives a larger value for  $\Delta\gamma_{data}$ . For the remaining 5 flares, the single-power-law function still gives a good fit to the spectrum with different background models. In summary, the uncertainties in  $\gamma_2$  that are associated with the assumed background model do not change our conclusions.

In the total of the 20 flares, 15 flares required a double power-law fit to the HXR photon spectrum above the thermal emission, while the other 5 flares did not show a significant break. Spectra and Pixon images for the 20 flares are shown in Figures 6, 7 and 8. The spectra in Figures 6 and 7 are shown with the best-fit for the step-function ionization model with the Haug cross section ( $I_H$ ). The single-power-law spectra in Figure 8 are shown with the best-fit single-power-law photon spectrum.

Notice that for flare No.2 in Figure 6, both the reduced  $\chi^2 = 3.44$  and the residuals indicate a poor fit. But for flare No.6, even though the value of reduced  $\chi^2$  is 0.93, the systematic variations at  $\sim 20\text{--}80$  keV in the residuals indicate a poor fit. This demonstrates that  $\chi^2$  alone is not an adequate indicator of an acceptable fit. An acceptable fit to the spectrum must have both a reduced  $\chi^2$  that is close to 1 and residuals that don't show systematic variation with photon energy.

For the 15 flares with a spectral break, a comparison of  $\Delta\gamma_{data}$  with  $\Delta\gamma_{model}$  is given in Figure 4. Each diamond indicates two parameters for each flare:  $\gamma_2+1$  (taken as an approximation to  $\delta$ ) and  $\Delta\gamma_{data}$  obtained from the double power-law photon fit. The error bars show the 95% confidence interval obtained from the Monte Carlo method. We did not use  $\delta$  from the nonuniform ionization fit because it is not meaningful when the fit is not good, though the formal uncertainty on  $\gamma_2$  is larger than that on  $\delta$ . Of these flares, 6 (30% of total, 40% of the flares with broken spectra) have values of  $\Delta\gamma_{data}$  that have less than 2.5% probability of being consistent with the upper limit of the model. They could not be acceptably fitted by the step-function nonuniform ionization model. As discussed in Section 3, they are inconsistent with any model with a more gradual change in degree of ionization with distance as well. Therefore, nonuniform ionization cannot explain the spectral flattening for these flares, because the spectra are too flattened below the break energy.

The next to the last column in Table 1 gives the statistical probability for each of the 15 flares with double power-law spectral fits being consistent with the upper limit for nonuniform ionization plotted in Figure 4. The flare 1 spectrum for example, is consistent with nonuniform ionization but has a 32% probability of being inconsistent with the model. By our criterion that to be inconsistent with nonuniform ionization the theoretical upper limit  $\Delta\gamma_{model}$  must be outside the 95% confidence interval for  $\Delta\gamma_{data}$ , flare 3 is also consistent with nonuniform ionization but has a 97% probability of being inconsistent with it. Flares 2, 6, 8, 9, 11 and 14 are all found to be inconsistent with nonuniform ionization.

The images at 40-60 keV show that of these six flares, three show a single source and the other three show double sources. For this sample, all flares (No. 2, 8, 11 and 12) that show only a single source at 40-60 keV have a spectral break  $\Delta\gamma_{data}$  in the range from 0.5 to 1.2. All the five flares without a spectral break shown in Figure 8 show two or three



sources. This may indicate that single sources are more likely to have a spectral break.

## 6. Summary and Discussion

We used two ionization profiles, a step function and a linear function, and a close approximation to the full Bethe-Heitler cross-section to investigate the possible effects of nonuniform ionization on HXR spectra. Compared with the fully ionized thick-target, nonuniform ionization in the thick-target region enhances the relative HXR bremsstrahlung flux by a factor of up to 2.8 at high energies (see also Kontar et al. 2002) and, therefore, causes a spectral flattening at energies below that at which the electrons lose all of their energy in the fully ionized region of the thick target. The Kramers approximation and the full cross-sections give photon spectral indexes that differ by up to 6.8%, fluxes that differ by up to 36%, and break energies that differ by 8% for electron distribution with  $\delta = 4$  (see Figures 1 and 2). The change in spectral index  $\Delta\gamma_{model} = \gamma_{model}^{max} - \gamma_{model}^{min}$  derived from the nonuniform ionization model, as a function of the electron distribution index  $\delta$ , gives an upper limit on  $\Delta\gamma_{data} = \gamma_2 - \gamma_1$  from a double power-law fit to the photon spectrum. A spectral break with a larger value of  $\Delta\gamma_{data}$  than this limit cannot be caused by nonuniform ionization alone.

We studied a sample of 20 limb flares from the *RHESSI* data base to estimate what fraction of flares have HXR spectral flattening that can or cannot be explained by nonuniform ionization alone. A Monte Carlo method was used to estimate the uncertainties in the fit parameters. In the sample of 20 flare spectra, 15 showed a significant break in the peak photon spectrum at energies above the range dominated by thermal emission. Values of  $\Delta\gamma_{data}$  were between 0.34 and 1.45 and the break energy between 31 and 107 keV. We find that at least 6 flares of these 15 cannot be explained by nonuniform ionization alone. They all have a value of  $\Delta\gamma_{data}$  with less than 2.5% probability of being consistent with the

computed upper limit (Figure 4). The linear ionization function gives less flattening of the spectra (smaller values of  $\Delta\gamma$ ) than the step function (Figures 1 and 2), and thus doesn’t help in explaining the large  $\Delta\gamma$  values obtained from observations. Another effect, such as return current losses, an injected broken power-law electron distribution, or a low-energy cutoff to the electron distribution, must be at least partially responsible for the spectral break in these ten flares.

Among these 6 flares that cannot be explained by nonuniform ionization alone, three show single compact sources at 40-60 keV and the other three show two sources. All the four flares that show a single source have a spectral break with  $\Delta\gamma$  between 0.5 and 1.2. All the five flares which do not have a spectral break show at least two sources. This suggests that the HXR emission from a single source is not likely to have a single-power-law photon spectrum. However, it is possible that some of the flares in our sample have another source region that is occulted by the limb. The spatial resolution of the Pixon images also varies for the flares. A compact source may show two or more sources if the spatial resolution were better. We will analyze the spectral differences of individual sources in future work.

For the 9 flares with a break that may be explained by nonuniform ionization, the values of  $E_*$  derived from the fits range from 25 to 100 keV, corresponding to column densities  $N_* = N_1$  (Equation 3) from  $9 \times 10^{19}$  to  $1.5 \times 10^{21} \text{ cm}^{-2}$ . These values are consistent with the results from Kontar et al. (2002) and Kontar et al. (2003), but are significantly larger than the value of  $1 \times 10^{19} \text{ cm}^{-2}$  where the ionization  $x$  drops to 0.5 for model F2 of Machado et al. (1980) (see also Kontar et al. 2003). The breaks in our sample flares require a greater column depth for the ionization transition level. The reason may be that RHESSI cannot observe smaller values of  $E_*$ , since the thermal emission always dominates at low energies at the HXR peak time, or that the upper chromosphere is already heated up at the HXR peak time, resulting in a deeper ionization transition level (greater column density in

the fully ionized part of the electron path).

For this paper, we analyzed a spectrum from only a single spin period time interval ( $\sim 4$  s) near the HXR peak of each flare. However, we know that the spectral shape changes during the evolution of a flare. For example, it may be a single power-law spectrum at the peak and a broken power-law in the rise phase, or on the decay. Further study of the temporal evolution of those flares and of other flares, including flares closer to disk center, will give more information to interpret the breaks in the photon spectra. The deduced time evolution of  $E_*$  and the column density  $N_*$  will be compared with expectations from chromospheric evaporation models. We will also study the changes in the locations of the HXR sources during the time when the spectra change from single power-law to double power-law or the reverse. Imaging spectroscopy will be used to investigate the spectral breaks in the individual sources. For the flares with spectra that have  $\Delta\gamma$  greater than that possible with any nonuniform ionization model, other mechanisms will be considered, such as return current losses, and deviations from a single power-law electron distribution.

We thank the *RHESSI* PI team for the excellence and easy availability of the data and the analysis software. Yang Su acknowledges NSF support through ATM-0725135. This work was supported in part by the RHESSI Project and a NASA HGI (Heliophysics Guest Investigator) grant.

*Facilities:* RHESSI.

## REFERENCES

- Brown, J. C. 1971, *Sol. Phys.*, 18, 489
- Brown, J. C. 1973, *Sol. Phys.*, 28, 151
- Brown, J. C., McArthur, G. K., & McIntosh, S. W. 1996, in *ASP Conf. Ser., Magnetic Reconnection in the Solar Atmosphere*, 111, ed. R. D. Bentley, & J. T. Mariska, 292
- Brown, J. C., McArthur, G. K., Barrett, R. K., McIntosh, S. W., & Emslie, A. G. 1998, *Sol. Phys.*, 179, 379
- Brown, J. C., Kašparová, J., Massone, A. M., & Piana, M. 2008, *A&A*, 486, 1023
- Dulk, G. A., Kiplinger, A. L., & Winglee, R. M. 1992, *ApJ*, 389, 756
- Gan, W. Q., Li, Y. P., Chang, J., & Tiernan, J. M. 2002, *Sol. Phys.*, 207, 137
- Haug, E. 1997, *A&A*, 326, 417
- Holman, G. D., Kundu, M. R., & Papadopoulos, K. 1982, *ApJ*, 257, 354
- Holman, G. D. 2003, *ApJ*, 586, 606
- Kašparová, J., Kontar, E. P., & Brown, J. C. 2007, *A&A*, 466, 705
- Kontar, E. P., Brown, J. C., & McArthur, G. K. 2002, *Sol. Phys.*, 210, 419
- Kontar, E. P., Brown, J. C., Emslie, A. G., & Schwartz, R. A. 2003, *ApJ*, 595, 123
- Kontar, E. P. & Brown, J. C. 2006, *ApJ*, 653, 149
- Kontar, E. P., MacKinnon, A. L., Schwartz, R. A., & Brown, J. C. 2006, *A&A*, 446, 1157
- Koch, H. W., & Motz, J. W. 1959, *Reviews of Modern Physics*, 31, 920

- Knight, J. W., Sturrock, & P. A. 1977, *ApJ*, 218, 306
- Krucker, S., & Lin, R. P. 2008, *ApJ*, 673, 1181
- Lin, R. P., & Schwartz, R. A. 1987, *ApJ*, 312, 462
- Lin, R. P., Dennis, B. R., Hurford, G. J., et al. 2002, *Sol. Phys.*, 210, 3
- Machado, M. E., Avrett, E. H., Vernazza, J. E., & Noyes, R. W. 1980, *ApJ*, 242, 336
- Massone, A. M. et al. 2004, *ApJ*, 613, 1233
- Melrose, D. B. 1990, *Sol. Phys.*, 130, 3
- Petrosian, V. 1973, *ApJ*, 186, 291
- Phillips, K. J. H. 2004, *ApJ*, 605, 921
- Smith, D. M., Lin, R. P., Turin, P., et al. 2002, *Sol. Phys.*, 210, 33
- Sui, L. H., Holman, G. D., & Dennis, B. R. 2007, *ApJ*, 670, 862
- Zhang, J., & Huang, G. L. 2004, *Sol. Phys.*, 219, 135
- Zharkova, V. V., & Gordovskyy, M. 2006, 651, 553

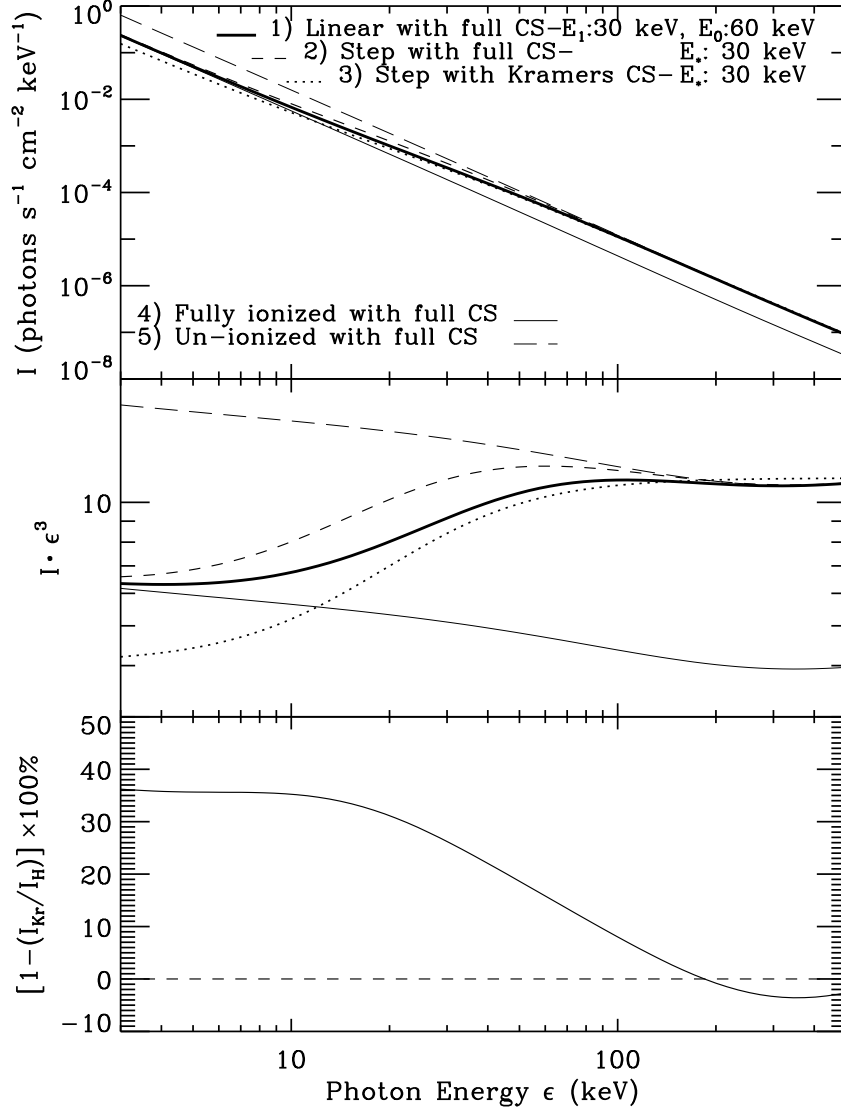


Fig. 1.— Comparison of the computed thick-target photon spectra from the following five nonuniform ionization models, all for a single power-law electron distribution function with  $\delta=4$ : (1) the linear ionization function with the full cross-section ( $I_H$ ) for  $E_1=30$  keV and  $E_0=60$  keV (*thick line*), (2) step function ionization with the full cross-section and  $E_*=30$  keV (*dashed line*), (3) step-function with the Kramers cross-section ( $I_{Kr}$ ) and  $E_*=30$  keV (*dotted line*), (4) a fully ionized thick target (*thin solid line*) and (5) an un-ionized thick target (*long dashed line*). *Top panel:* the photon spectra as a function of  $\epsilon$ . *Middle panel:* photon spectra multiplied by  $\epsilon^3$  to better show the differences. *Bottom panel:* the percentage difference between the step-function results with the full cross-section ( $I_H$ ) and with the Kramers approximation ( $I_{Kr}$ ).

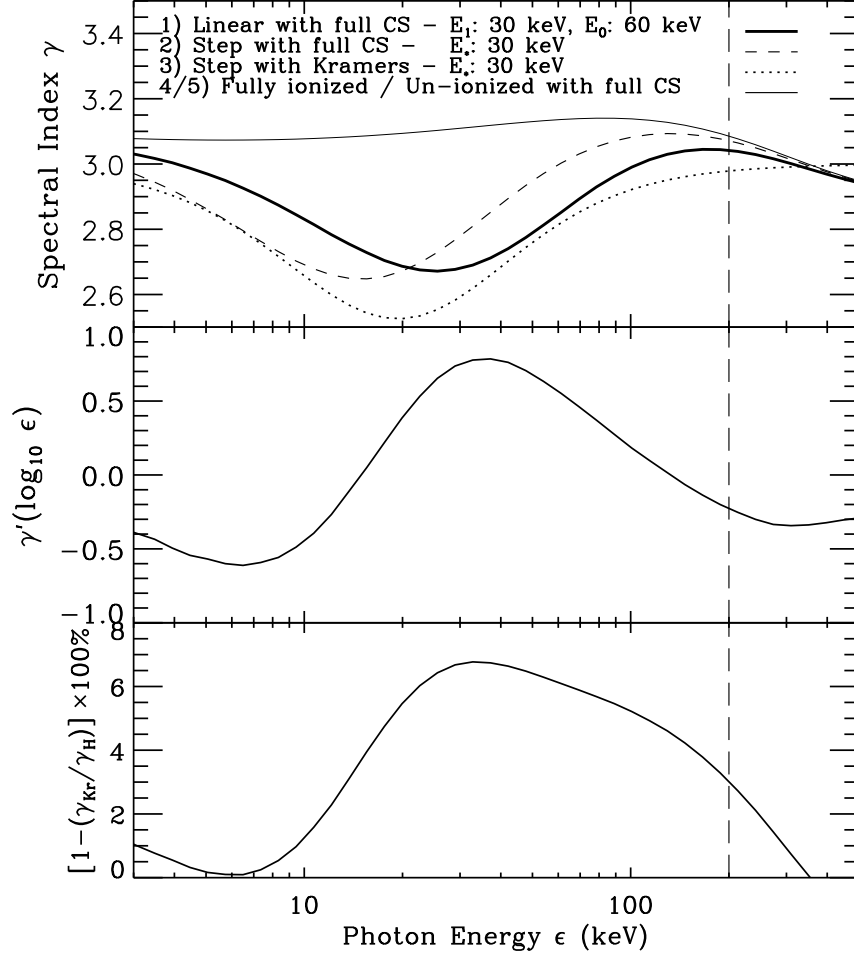


Fig. 2.— *Top panel:* Spectral index  $\gamma$  of photon spectra as a function of  $\epsilon$  for the five models in Figure 1. The power-law index for electrons,  $\delta$ , is 4. *Middle panel:* The derivative of  $\gamma(\log_{10}\epsilon)$ ,  $d\gamma(\log_{10}\epsilon)/d(\log_{10}\epsilon)$ , for the step-function model with full cross-section. *Bottom panel:* the percentage difference of  $\gamma$  between the step-function results with the full and Kramers cross-sections. The vertical dashed line at 200 keV shows the upper end of the energy range used for fit to the measured photon spectra in this paper.

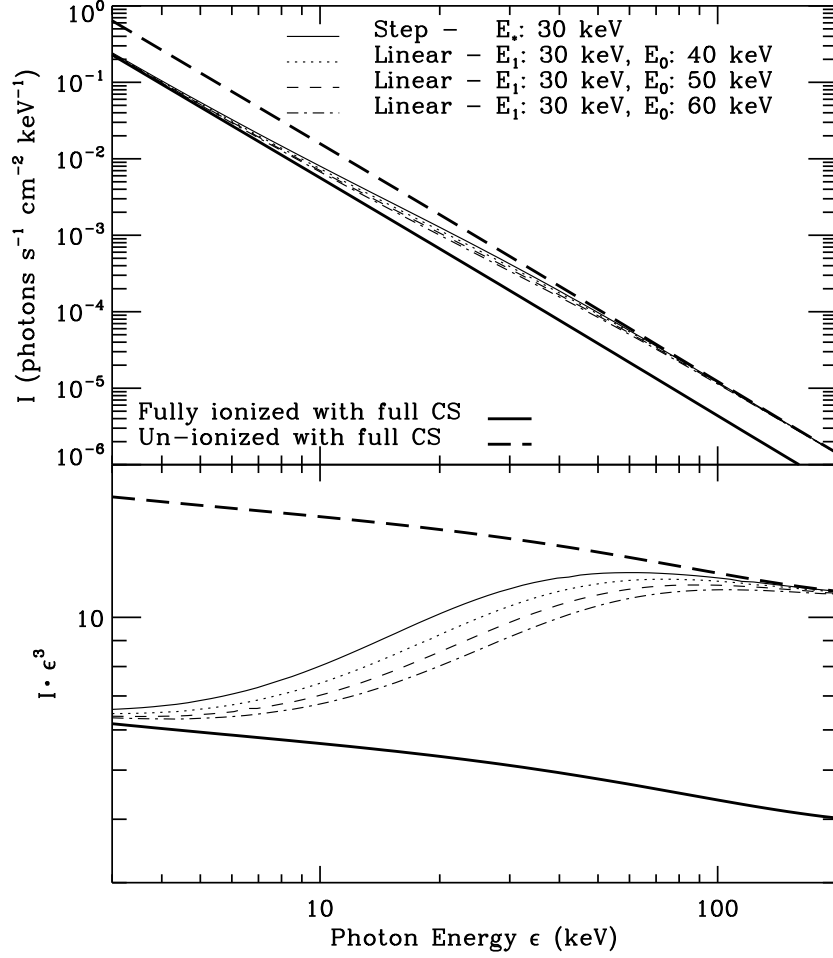


Fig. 3.— *Top panel:* comparison of spectra from the linear-ionization function model with  $E_0 = 30$  keV and three different values of  $E_0$  (40, 50, and 60 keV). The thick solid line shows the spectrum from a fully ionized thick target and the thick long-dash line shows the un-ionized model. The thin line shows the step-function model for  $E_* = 30$  keV. All are for  $\delta = 4$  with full cross-section. *Bottom panel:* same as middle panel of Figure 1, photon spectra multiplied by  $\epsilon^3$  to better show the differences.



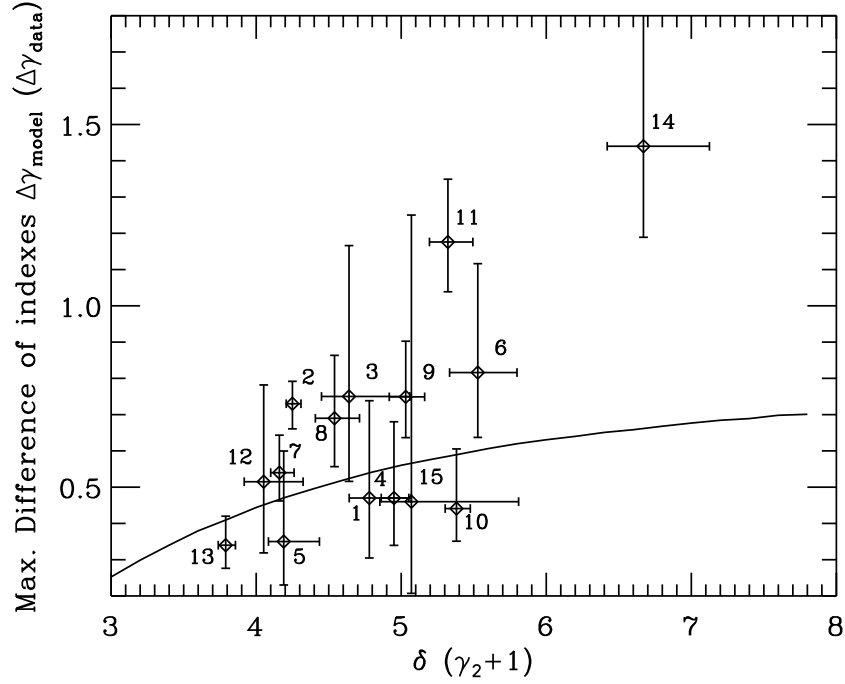


Fig. 4.— The curve shows the upper limits  $\Delta\gamma_{\text{model}}$ , predicted from the step-function model with full cross-section (see Section 3), as a function of  $\delta$ , the electron power-law distribution index. The diamonds show the values of  $\Delta\gamma_{\text{data}}$  obtained from the fit results for flares 1–15 in Table 1 (also see section 5). The measured  $\Delta\gamma_{\text{data}}$  for each data point is from a broken power-law fit to the spectra and  $\gamma_2 + 1$  is an approximation to  $\delta$ . The error bars showing the 95% confidence intervals in  $\Delta\gamma_{\text{data}}$  and  $\gamma_2 + 1$  were obtained from the Monte Carlo method described in the text.

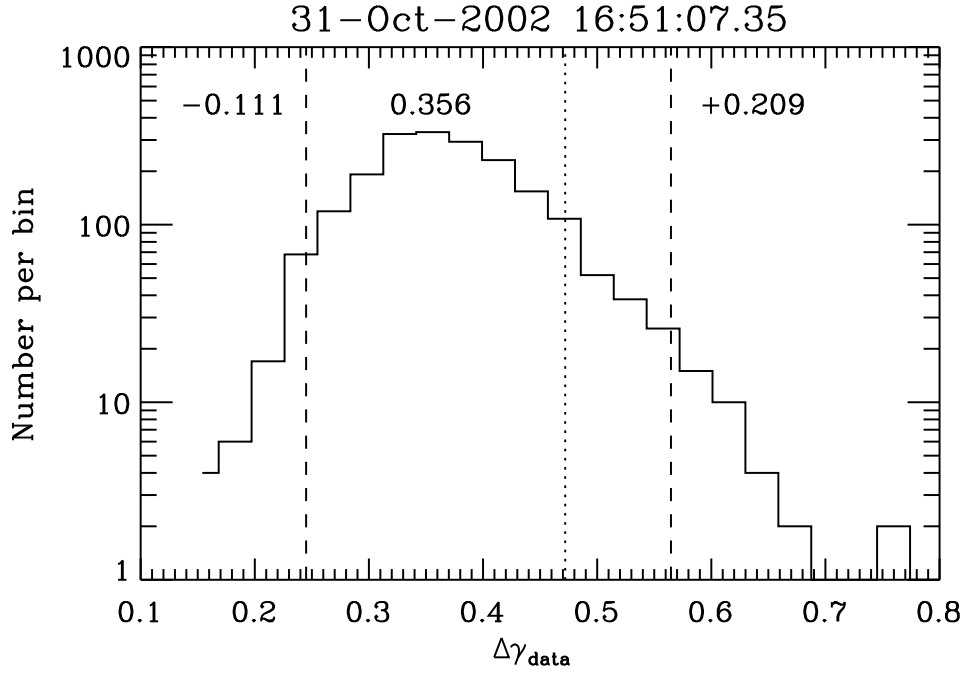


Fig. 5.— Example of the distribution of  $\Delta\gamma_{\text{data}}=\gamma_2-\gamma_1$  from the Monte Carlo program. The two dashed lines show the 95% confidence range (2.5% in each tail). The numbers give the peak (most probable) value (0.356) of  $\Delta\gamma_{\text{data}}$  and the lower and upper uncertainties on this peak value (about  $\pm 2\sigma$ ). The dotted line gives the location of the corresponding upper limit  $\Delta\gamma_{\text{model}}$  (see Figure 4) obtained from the nonuniform ionization model for this flare (No. 5 in Table 1).

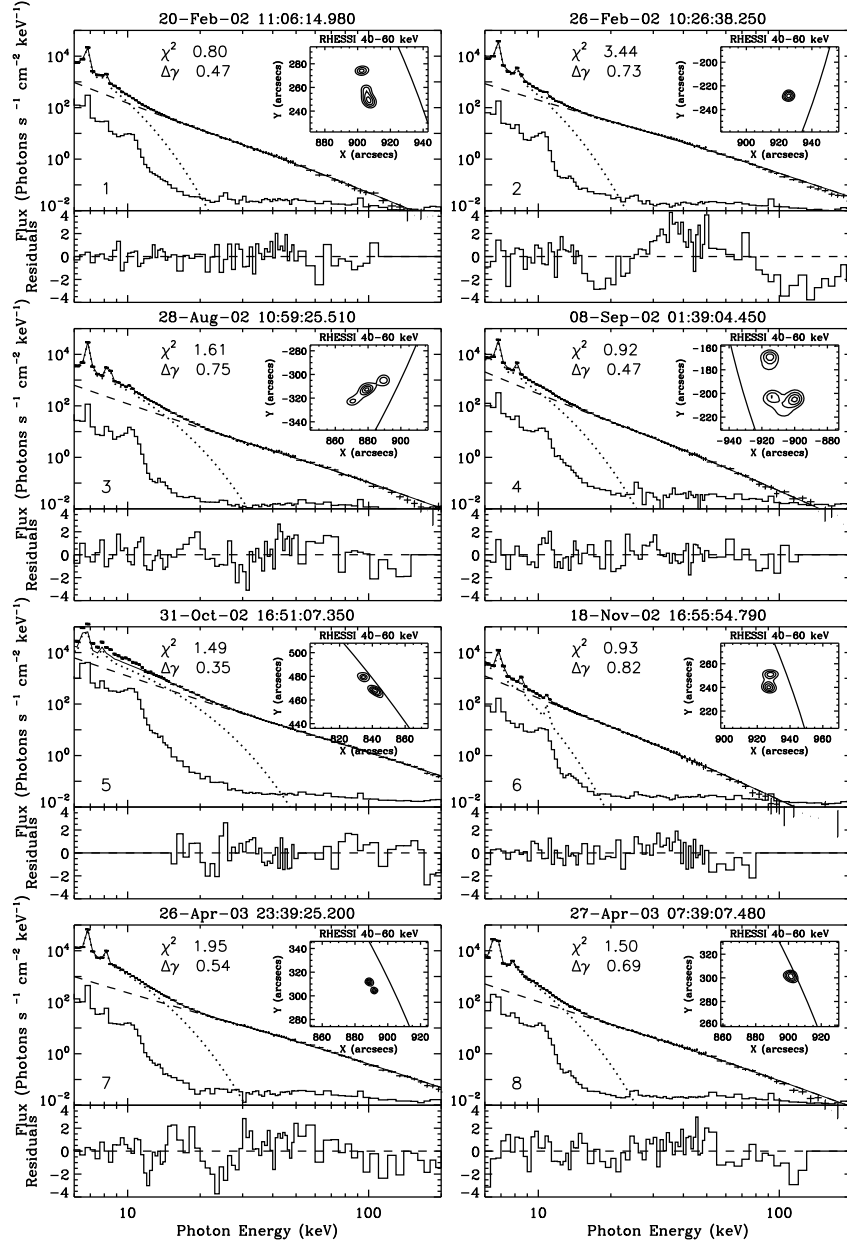


Fig. 6.— Spectral fits for flares 1–8 from Table 1. The spectra are fitted by isothermal emission (*dotted line*) and the step-function ionization model with full cross-section ( $I_H$ ) (*dashed line*). The fit residuals,  $(\text{observed} - \text{model})/\sigma_{\text{model}}$ , are shown below each spectrum. The Pixion images for the 40–60 keV band and the same one-spin time intervals as for these spectra are shown as contours at 30%, 50%, 70%, and 90% of the maximum flux.

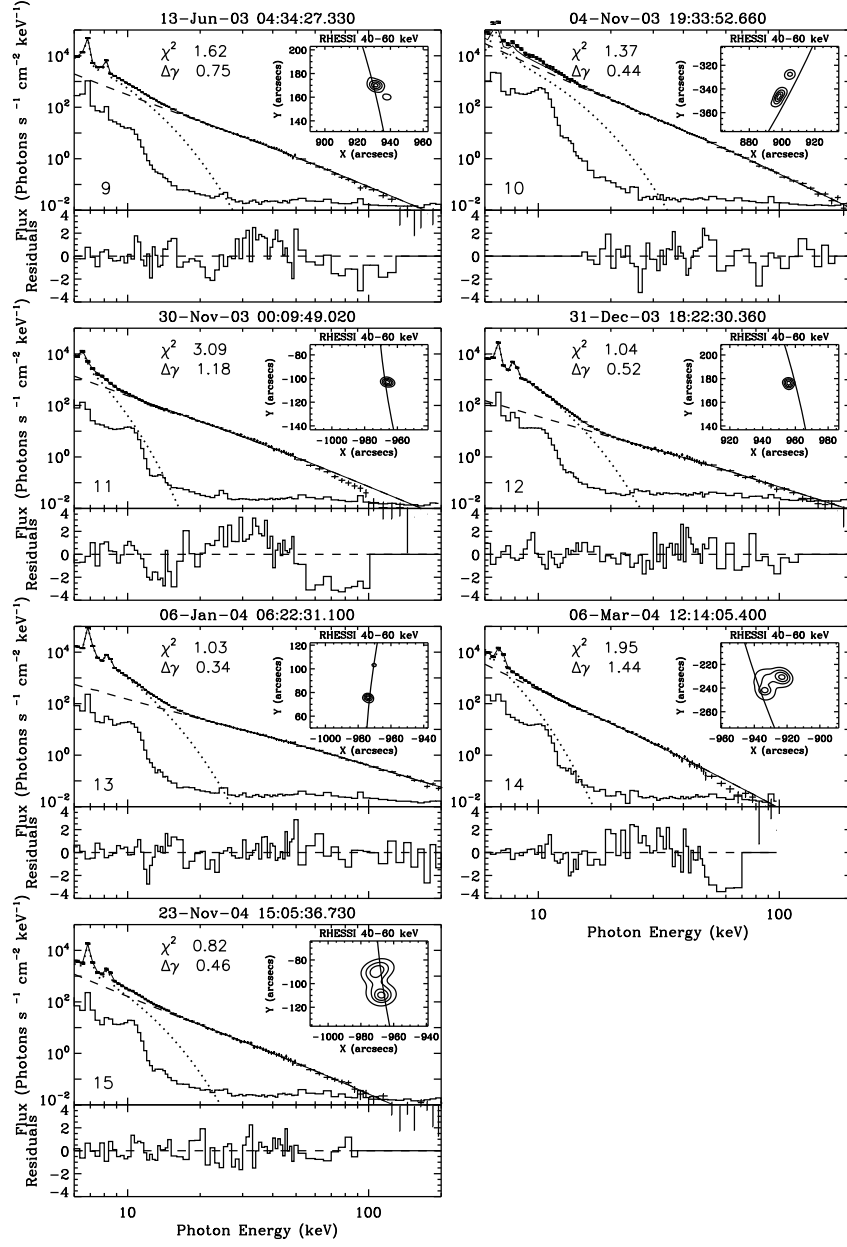


Fig. 7.— Same as Figure 6, but for flares 9–15.

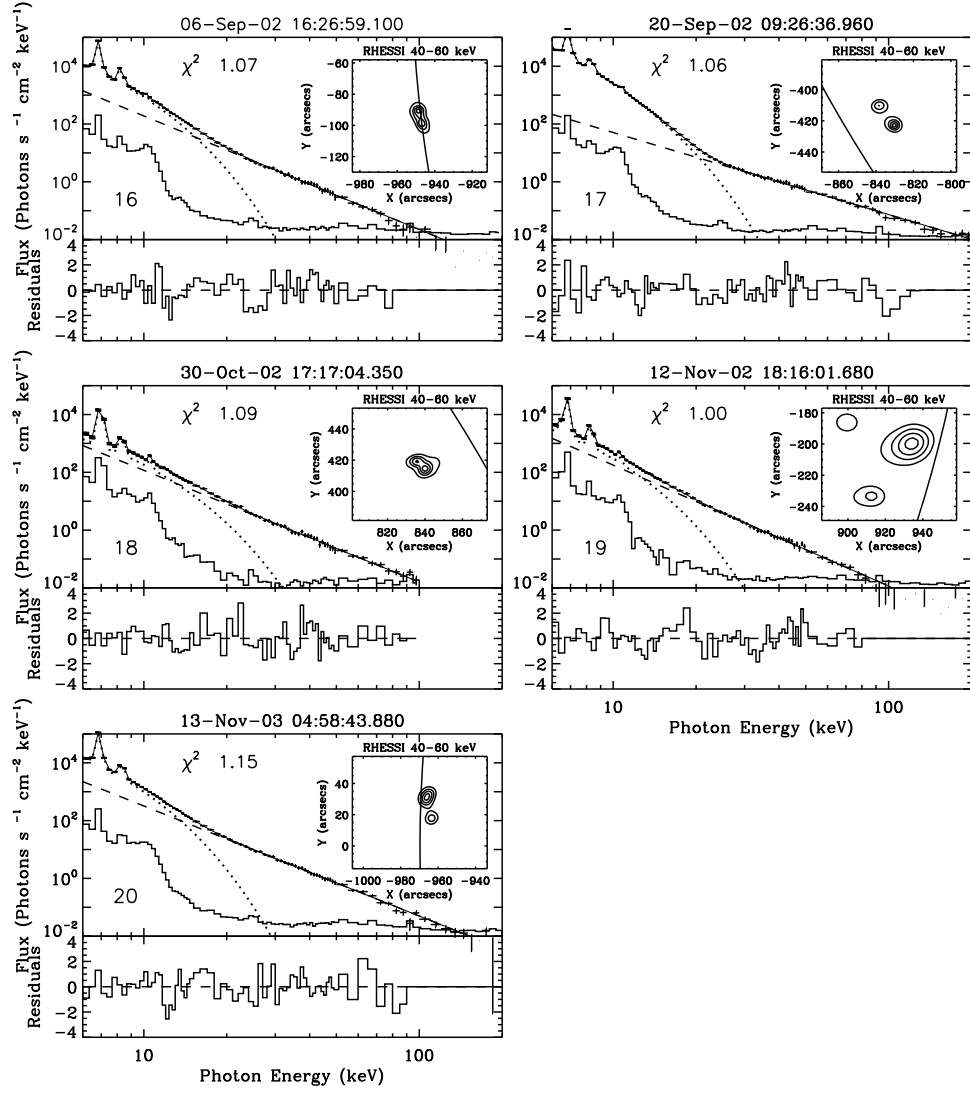


Fig. 8.— Similar to Figure 6 but for flares 16–20 from Table 1. The nonthermal component of the fitted spectra in these cases is from a single-power law photon fit.

Table 1. Flares Parameters

	Start Time of Flare Spectrum	Double Power-law			Step with $I_{Kr}$			Step with $I_H$			Nonuniform	Source
		$\Delta\gamma$	$E_{bk}$	$\chi^2$	$\delta_{Kr}$	$E_*$	$\chi^2$	$\delta_H$	$E_*$	$\chi^2$	Ionization ?	
1	20-Feb-2002 11:06:14.98	0.47	45.4	0.73	4.86	27.9	0.82	4.71	35.6	0.80	68%	D
2	26-Feb-2002 10:26:38.25	0.72	41.9	1.21	4.18	29.7	3.31	4.05	38.3	3.44	< 2.5%	S
3	28-Aug-2002 10:59:25.51	0.75	71.4	1.38	4.46	46.0	1.58	4.29	57.8	1.61	2.9%	M
4	8-Sep-2002 01:39:04.45	0.47	30.5	0.91	5.14	21.5	0.94	4.99	25.0	0.92	76%	M
5	31-Oct-2002 16:51:07.35	0.35	107.2	1.44	4.35	81.5	1.39	4.17	100.1	1.49	86%	D
6	18-Nov-2002 16:55:54.79	0.82	36.2	0.63	5.29	17.0	0.95	5.13	18.8	0.93	< 2.5%	D
7	26-Apr-2003 23:39:25.20	0.54	58.3	1.51	4.14	37.9	1.90	3.98	45.1	1.95	3.4%	D
8	27-Apr-2003 07:39:07.48	0.69	45.7	1.11	4.43	27.3	1.51	4.28	33.6	1.50	< 2.5%	S
9	13-Jun-2003 04:34:27.33	0.75	41.3	0.94	4.95	24.9	1.68	4.79	29.0	1.62	< 2.5%	D
10	4-Nov-2003 19:33:52.66	0.44	49.4	1.25	5.52	27.3	1.43	5.35	32.1	1.37	97%	D
11	30-Nov-2003 00:09:49.02	1.18	35.9	0.95	4.82	17.8	3.16	4.70	21.9	3.09	< 2.5%	S
12	31-Dec-2003 18:22:30.36	0.52	44.5	0.93	4.11	35.9	1.03	3.95	42.8	1.04	23%	S
13	6-Jan-2004 06:22:31.10	0.34	49.1	0.99	3.93	39.7	0.98	3.78	50.5	1.03	96%	D
14	6-Mar-2004 12:14:05.40	1.45	33.4	1.00	5.90	14.3	2.01	5.76	16.1	1.95	< 2.5%	D
15	23-Nov-2004 15:05:36.73	0.46	42.9	0.80	5.18	25.9	0.83	5.01	29.0	0.82	62%	D
		$\gamma$		$\chi^2$								Image
16	6-Sep-2002 16:26:59.10	3.93		1.07	...	...	...	...	...	...	...	D
17	20-Sep-2002 09:26:36.96	2.84		1.06	...	...	...	...	...	...	...	D
18	30-Oct-2002 17:17:04.35	3.87		1.09	...	...	...	...	...	...	...	D
19	12-Nov-2002 18:16:01.68	4.18		1.00	...	...	...	...	...	...	...	M
20	13-Nov-2003 04:58:43.88	3.81		1.15	...	...	...	...	...	...	...	D

\*The time is the start time of the fit time interval ( $\sim 4$  s). The fit results are for three models, from left to right: a double-power law, step function with Kramers cross-section, and step function with full cross-section. Flares 1-15 required a broken power-law. Flares 16-20 could be fit with a single power-law. “Nonuniform Ionization?” indicates the percentage probability of consistency, obtained from the Monte Carlo method, between the measured photon spectrum and the nonuniform ionization model for each flare. The column “Source” gives the number of major emission regions at 40-60 keV for each flare. S, D and M mean single, double and multiple, respectively. Two isothermal functions, in addition to a power-law, were used to get an acceptable fit for flare No.17. The  $\chi^2$  used in this table is the reduced  $\chi^2$ .